Chemical Engineering Journal Advances 11 (2022) 100340

Contents lists available at ScienceDirect

Chemical Engineering Journal Advances

journal homepage: www.sciencedirect.com/journal/chemical-engineering-journal-advances

CC3 porous organic cage crystals and membranes for the non-thermal plasma catalytic ammonia synthesis

Fnu Gorky [a], Hoang M. Nguyen [c], Jolie M. Lucero [b], Shelby Guthrie [a], James M. Crawford [b], Moises A. Carreon [b,*], Maria L. Carreon [c,*]

[a] Chemical and Biological Engineering Department, South Dakota School of Mines & Technology, 501 E Saint Joseph St, Rapid City, SD, 57701, USA
[b] Chemical and Biological Engineering Department, Colorado School of Mines, Golden, CO, 80401, USA
[c] Mechanical Engineering Department, University of Massachusetts Lowell, Lowell, MA, 01854, USA

ARTICLE INFO

Keywords:
Non-thermal plasma
Plasma catalysis
Ammonia synthesis
Porous organic cages
Advanced porous catalyst
Membranes

ABSTRACT

Ammonia is considered a basic building block for fertilizers. Also, it is an economically efficient and technologically suitable solution for energy storage and transportation. Non-thermal plasma-driven catalysis powered by renewable energy is considered as a green alternative to the conventional Haber-Bosch process for ammonia synthesis. The main challenge in this electron-mediated route is the low ammonia synthesis production, given the plasma-induced decomposition of the freshly generated ammonia during the reaction. Herein we report the plasma-assisted ammonia synthesis in a dielectric barrier discharge reactor packed with CC3 crystals, a prototypical porous organic cage, and a molecular-sieve membrane fabricated from the same CC3 material. The CC3 crystals delivered the highest ammonia synthesis rate (0.06 μmol min^{-1} m^{-2}) compared to other microporous catalysts such as zeolite (SAPO-34) and metal-organic frameworks (ZIF-8, ZIF-67) (below 0.02 μmol min^{-1} m^{-2}). The CC3 porous cage with well-defined octahedral crystal geometry provides partial protection while the CC3 membrane offers both adsorption and separation effects for the freshly formed ammonia from its in-situ decomposition, securing an excellent ammonia synthesis rate of 20.3 μmol min^{-1} m^{-2}. The findings from this work unfolds novel insights into rational designs of advanced porous catalyst and membrane for plasma-driven catalytic ammonia synthesis in a sustainable and efficient way.

1. Introduction

Ammonia (NH_3) is one of the most foundational chemical feedstocks, as it is considered not only an indispensable precursor for fertilizers, pharmaceuticals, dyes but also as a crucial energy storage medium and carbon-free energy carrier[1]. Ammonia can be decomposed to supply CO_x-free hydrogen for various application, including hydrogen fuel cell, ammonia fuel cell, or catalytic ammonia combustion[2]. Recently, automobiles operating on pure ammonia and gasoline-ammonia fuel modifications are being hypothesized and on the verge of being prototyped[3]. An important advantage of using pure ammonia is the resulting diminished reliability on fossil fuels by changing to a "sustainable fuel source" that can be manufactured synthetically[4]. Nonetheless, artificial nitrogen fixation to ammonia remains a significant limitation in the sustainable development of society. Intensive efforts have been paid to optimize the prevalent Haber-Bosch (H-B) ammonia synthesis process for large-scale production. Although this century-old technology requires harsh operating conditions such as high reaction temperature (400–500 °C) and high pressure (150–300 atm)[5]. As a consequence this process accounts for about 1–2% of global emissions [6]. Such large intrinsic carbon footprint technology for ammonia synthesis highlights the significant importance for the development of alternative processes that operate under milder conditions such as atmospheric pressure and preferably with zero carbon emissions.

One of the most promising routes to achieve this goal is the use of decentralized synthesis processes powered by renewable electricity, which can even exploit benefits from local resources in remote regions. Electron-based technologies such as non-thermal plasma (NTP) powered by renewables are among such processes. NTP offers high-energy electrons, exciting the ground state gas molecules to participate and react effectively on selective surfaces at lower temperature and atmospheric pressure, which contrasts to the energy-intensive thermal catalysis route [7–9]. Moreover, plasma reactors have the added advantage of potentially being operated by renewable electricity sources (wind and solar),

* Corresponding authors.
E-mail addresses: mcarreon@mines.edu (M.A. Carreon), maria_carreon@uml.edu (M.L. Carreon).

https://doi.org/10.1016/j.ceja.2022.100340

Available online 9 June 2022

offering a sustainable solution[10]. These intermittent sources can be adapted to plasma power supplies, suggesting solutions like pulse-width modulation, effortlessly being switched on/off[11]. This possible electrification of the chemical industry can lead to small-scale independent ammonia production units to harness local supplies and provide economical solutions which have been omitted until now. NTP works efficiently with the N_2 activation for the production of ammonia without a catalyst[12]. Nonetheless, high ammonia production and selectivity are only secured with the presence of a suitable material[13–15]. Currently, the significant limitation of ammonia synthesis with NTP routes is the low ammonia synthesis rate derived from the in-situ decomposition of ammonia products in the plasma regime. In fact, upon modeling results, Van 't Veer et al.[16]. indicated that ammonia product generated in the plasma is decomposed during the micro-discharges *via* electron impact dissociation, while the ammonia is generated from N_2* and H* species during the afterglow. Other researchers also observed from an experimental study that the decomposition of ammonia product takes place simultaneously with its formation in the plasma[17, 18]. In plasma-mediated catalysis ammonia synthesis, our group have explored the good catalytic performance of a variety of microporous catalysts involving metal-organic frameworks[19, 20], and zeolites[12, 21]. These reports highlight the importance of the pore size and the framework in ammonia production. Lately, ZIF-21 membranes have provided a remarkable understanding of ammonia/nitrogen, and ammonia/hydrogen separation. Distinctively due to the polar-polar interactions between ammonia and the ZIF-21 linker polar channel leading to higher ammonia adsorption[22]. The observed pore size and framework composition effects prompted this work. Porous organic cage (POCs) materials have been gaining recent interest due to their desirable properties such as uniform pore size, higher surface areas, thermal and chemical stability[23, 24]. POCs have a unique solid-state molecular packing in contrast to other microporous materials, like carbon molecular sieves, metal-organic framework, porous polymers, and zeolites [23–27]. POCs configuration displays 3D connectivity via covalent bonding among organic cages which assembles them into microporous phases[23, 24]. Among POCs, CC3 is a widely studied prototype, with an exclusive porous crystalline structure and limiting pore size of ~3.6 Å, developed by coordination between 1,3,5-triformylbenzene and trans-1, 2-diaminocyclohexane[23–28]. The morphology of POCs like CC3 can be tunned during the synthesis process, labeling them as an asset in various applications[29]. More importantly, Cooper and co-workers demonstrated that the CC3 crystals can be used to fabricate a thin-film membrane by depositing the CC3 precursor solution on an aluminium support, and the primary results indicated a good selective gas separation[25]. Notwithstanding, none of the present-day studies report the use of CC3 in either powder or membrane form for ammonia synthesis. Most of the current research on POC materials has focused on the synthesis and characterization of the CC3 crystals to provide expectations on their promising performance in catalytic processes.

Herein the performance of CC3 in crystal and membrane forms for ammonia synthesis under NTP is evaluated. A typical zeolite (SAPO-34) and MOF catalysts (ZIF-8 and ZIF-67) are also employed to benchmark the performance of the CC3. An insight on the possible mechanism responsible for the observed improvement in the ammonia synthesis rate when employing the CC3 crystals and CC3 membrane is provided. This work aims to propose efficient approaches to tackle the current problems associated with the in-situ decomposition of ammonia product under NTP and therefore, providing the significant premise for practical applications of light-weight catalytic plasma membrane systems for island/decentralized areas, where plentiful renewable energy such as wind or solar can be integrated to operate such plasma-assisted processes.

2. Material and methods

2.1. CC3 crystals and CC3 membrane preparation

2.1.1. Synthesis of CC3 crystals

CC3 crystals were synthesized as reported in our previous work[30]. In brief, 15 mL of dichloromethane (Fisher Scientific, reagent grade) was added to 1 g of 1,3,5-triflormylbenzene (ACROS, 98%). In a second solution, 1.14 g of (±)-*trans*-1,2-diaminocyclohexane (ACROS, 98%) was homogenously dissolved in 15 mL of dichloromethane. The two solutions were then mixed and added to a Teflon-lined stainless-steel autoclave and treated at 50 °C for 48 h. The resultant crystals were recovered through centrifugation and washed with a 95:5 ethanol/DCM solution. The crystals were then dried in an oven at 100 °C. Other microporous materials with similar limiting pore aperture as CC3 were synthesized for comparison, following reported protocols: SAPO-34[31], ZIF-8[32], and ZIF-67[33]. Details on the synthesis of SAPO-34, ZIF-8, and ZIF-67 are described in the Supplementary Material.

2.1.2. Preparation of the CC3 membrane gel

CC3 gel was procured by the addition of two solutions. Firstly, 15 mL Dichloromethane was gradually added to 40 mg of 1,3,5- triformylbenzene in a Teflon-based liner, further 100 μL of trifluoroacetic acid was added. In parallel a homogenous solution of 15 mL of dichloromethane with 45 mg of (±)-trans-1,2-diaminocyclohexane was prepared, prior to incorporation in the Teflon liner.

2.1.3. Preparation of CC3 membranes

CC3 membranes were prepared by secondary seeded growth method inside the surface of porous α-Al_2O_3 tubes. The 6 cm supports (Inopor GmbH) have an inside diameter of 0.7 cm and an outside diameter of 1.1 cm and are asymmetric within the inner layer, which has a pore size of 100 nm. The effective support area was ~7.0–7.5 cm^2.

Initially, two bare cylindrical alumina supports were seeded with pre-prepared seeds. Following, the suspension of 20 mg of seeds in dichloromethane was further sonicated for at least 5–10 min. The peripheral regions of bare alumina support were covered with Teflon tape, prior to thermal treatment at 100 °C in the oven. After 5 min, the support was removed, and a pipette was used to drop the seeding solution on the inside of the hot support. To ensure the complete coverage of CC3 on the support, the procedure was replicated 3–4 times. The seeded supports were dried out at 80 °C overnight. The supports were removed from the oven and cooled down at room temperature before being added to the Teflon liner containing the mother gel. Then the autoclave was sealed and placed in a Vulcan furnace at 50 °C for 48 h for complete solvothermal synthesis. The autoclave was removed after 48 h and naturally cooled down to room temperature. The membranes were carefully rinsed with ethanol and dried overnight on a benchtop prior to thermal treatment in an oven at 150 °C. A second layer was then added to the initial layer by undergoing a second hydrothermal synthesis step and making a new membrane gel solution.

2.2. Catalyst characterization

The crystallinity of the prepared catalyst samples was examined *via* Powder X-ray diffraction analysis by using a Siemens Krystalloflex 810 operated at 25 mA and 30 kV. The morphology of the catalysts was characterized via scanning electron microscopy images (SEM) by using a JSM Field Emission microscope (JEOL-7000). The SEM images were collected at accelerating voltages of 8–15 kV. Nitrogen isotherms were performed on an ASAP 2020 Plus (Micromeritics) using a liquid nitrogen bath at 77 K. Samples were degassed for 8 h at 200 °C under high vacuum conditions. After degassing, the final weight was recorded. All samples were again degassed under high vacuum for 2 h on the analysis port prior to data acquisition. Surface areas were evaluated by using the Brunauer-Emmett-Teller method. Ammonia isotherms were compiled

on an ASAP 2020 apparatus (Micromeritics) equipped with corrosion resistant Kalrez® O-rings (DuPont™). Prior to analysis, samples were degassed under vacuum for at least 24 h. The ZIF-8, ZIF-67, and CC3 samples were degassed at 200 °C and SAPO-34 was degassed at 300 °C. A vacuum insulated Dewar with an ice bath at 273 K with equilibration times of at least 10 min was used for all samples.

2.3. Plasma-driven catalytic ammonia synthesis: the reactors employed

2.3.1. Packed DBD (dielectric barrier discharge) reactor

The catalytic activity of the CC3 crystals for ammonia synthesis was evaluated in a custom packed-bed DBD setup as shown in Fig. 1**(a).** The setup comprises four main parts: (i) the reactor core, (ii) the optical emission spectra (OES) capture setup, (iii) the electrical characterization setup; and (iv) the gas chromatography (GC) employed to follow the catalytic activity by identifying the products at the exit gas stream. To perform the catalytic tests, nitrogen and hydrogen gases were connected to the reactor through gas mass flow controllers. The quantification was performed using an Agilent 7820A GC equipped with an HP-PLOTU column (30 m x 0.32 mm x 10 μm) with hydrogen as a carrier. The gases were bubbled in deionized water to ensure all ammonia is captured and to perform titration as an alternate method of quantification. The high voltage power supply was connected to the reactor using Litz wire and alligator clips. The inner electrode made of a tungsten rod (2.4 mm diameter) was placed concentrically to the quartz tube with an I.D. of 4 mm and O.D. of 6.40 mm. The outer electrode was made of tinned copper mesh and acted as a ground electrode. The plasma zone length in this setup is approximately 8 cm. The gases flow through the annular region between the quartz tube and the inner electrode. Two quartz frits were placed carefully to avoid the catalyst powder displacement. 100 mg of catalyst were loaded in the form of fine powder in the annular section of the reactor. The reactions were carried out at

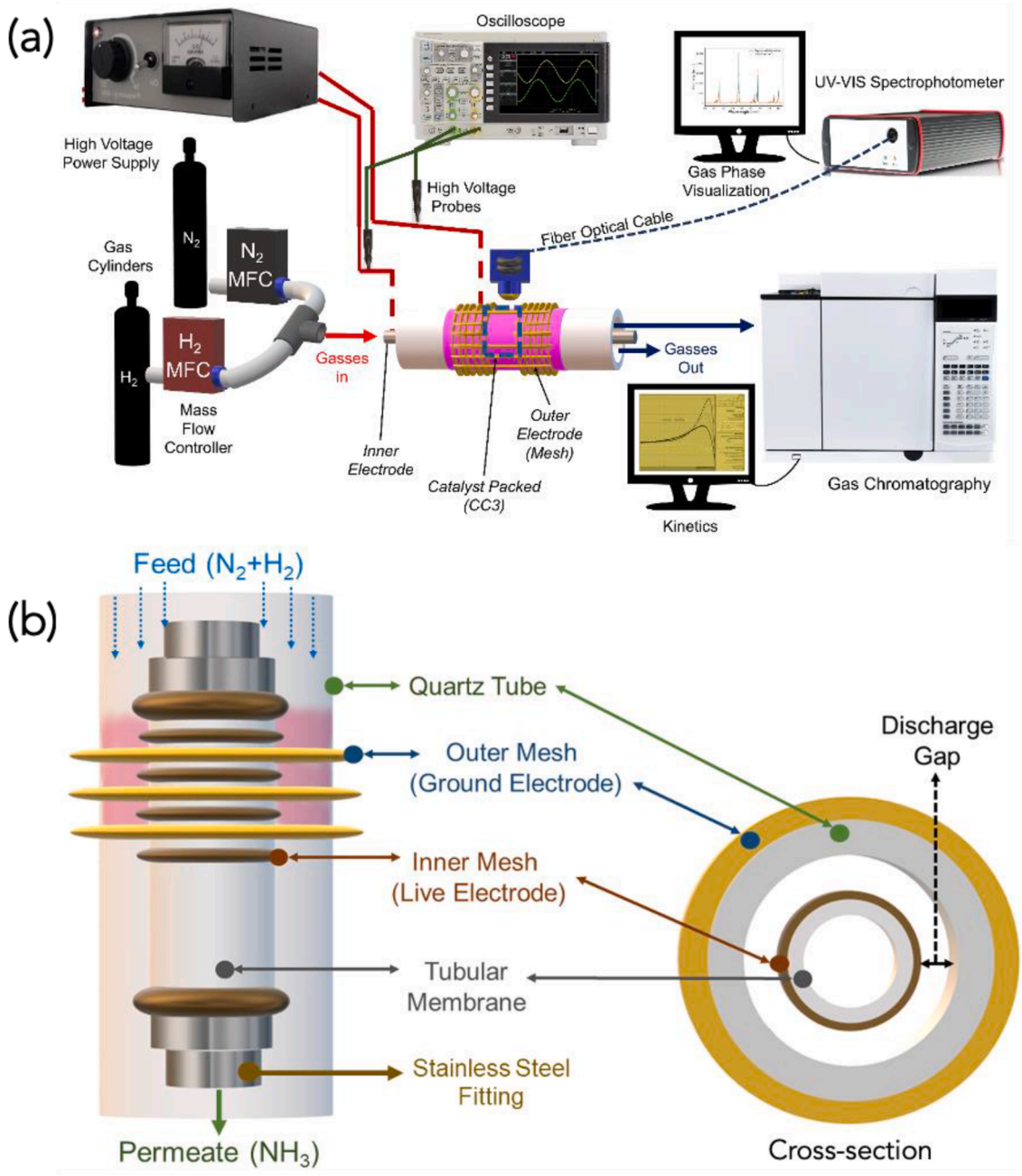

Fig. 1. Schematic of (a) DBD reactor packed with CC3 powder; and (b) the CC3 membrane reactor employed in this work.

different feed flow rates ranging from 3:1 to 1:6 ratio of nitrogen to hydrogen (N_2:H_2) and a total flow rate of 25 sccm at a constant voltage of 30 kV. To determine the ammonia synthesis rate, the reactor exhaust gas was sent to the gas chromatograph (GC) calibrated for ammonia synthesis. The calibration details are provided in the Supporting Information (**Table S1 and Figure S1**). The reactor was connected to an oscilloscope to obtain the current and voltage waveforms. A Tektronix 2048 series oscilloscope was used along with a Tektronix P6015A high voltage probe having a 1000X voltage reducing rating. The current was measured by a 10X current reducing probe to get the waveforms. The energy delivered to the reactor was calculated using these measurements. The emission spectra of the glow region were measured at the overlap region between the two electrodes. The measurements were recorded using a dual-channel UV–VIS-NIR spectrophotometer in scope mode (Avantes Inc., USB2000 Series). The spectral range was 200–1100 nm, with a line grating of 600 lines/mm and a resolution of 0.4 nm. A bifurcated fiber optic cable with 400 μm was employed.

2.3.2. Separator membrane reactor

The experimental steps used for the evaluation of the catalytic performance of the CC3 membrane are similar to those used for the tests over the packed DBD reactor as mentioned above. The detailed membrane reactor system is shown in

Fig. 1**(b)**. Due to the favourable energetic behavior of the CC3 crystals, we synthesized CC3 membranes grown on porous alumina tubular supports, which act as the reactor core. This plasma membrane reactor was uniquely designed as a post-plasma system with the purpose of enhancing the lifetime of the CC3 and avoiding the structural damage due to plasma active species collision observed in the crystals. Added to the benefit of adsorbing the fresh ammonia formed in the plasma zone on the CC3 membrane. In this set up the porous alumina cylindrical support was connected through stainless steel fittings to a stainless-steel tube that helps to support and acts as a live electrode. The stainless-steel fittings and the outer membrane support were covered with tinned copper mesh for creating the plasma discharge. The setup was supported in a quartz tube acting as dielectric and where the outer mesh (ground-electrode) was placed. The plasma was generated at the interface quartz-porous alumina outer cylindrical area (where the reaction occurs), while the membrane is deposited in the inner cylindrical area of the porous alumina acting as an ammonia reservoir. All the experiments were performed at atmospheric pressure.

3. Results and discussion

3.1. Catalyst characterization

The characterization results of the CC3 crystals are shown in Fig. 2**.** The CC3 crystalline domain of the CC3α was verified *via* the diffraction peaks at 2θ of 6.2°, 12.4°, 15.5°, 17.5°, 18.6°, 20.2°, 21.2°, 23.6°, 27.5°, and 31.2° (Fig. 2**(a)**). The XRD result is consistent with other researchers [34, 35]. To elucidate the CC3 phase observed in the experiments and the nature of the contraction–expansion, we compared experimental patterns with the simulated XRD patterns on *in silico* structures of CC3 structure with different theoretical degrees of expansions. Percent

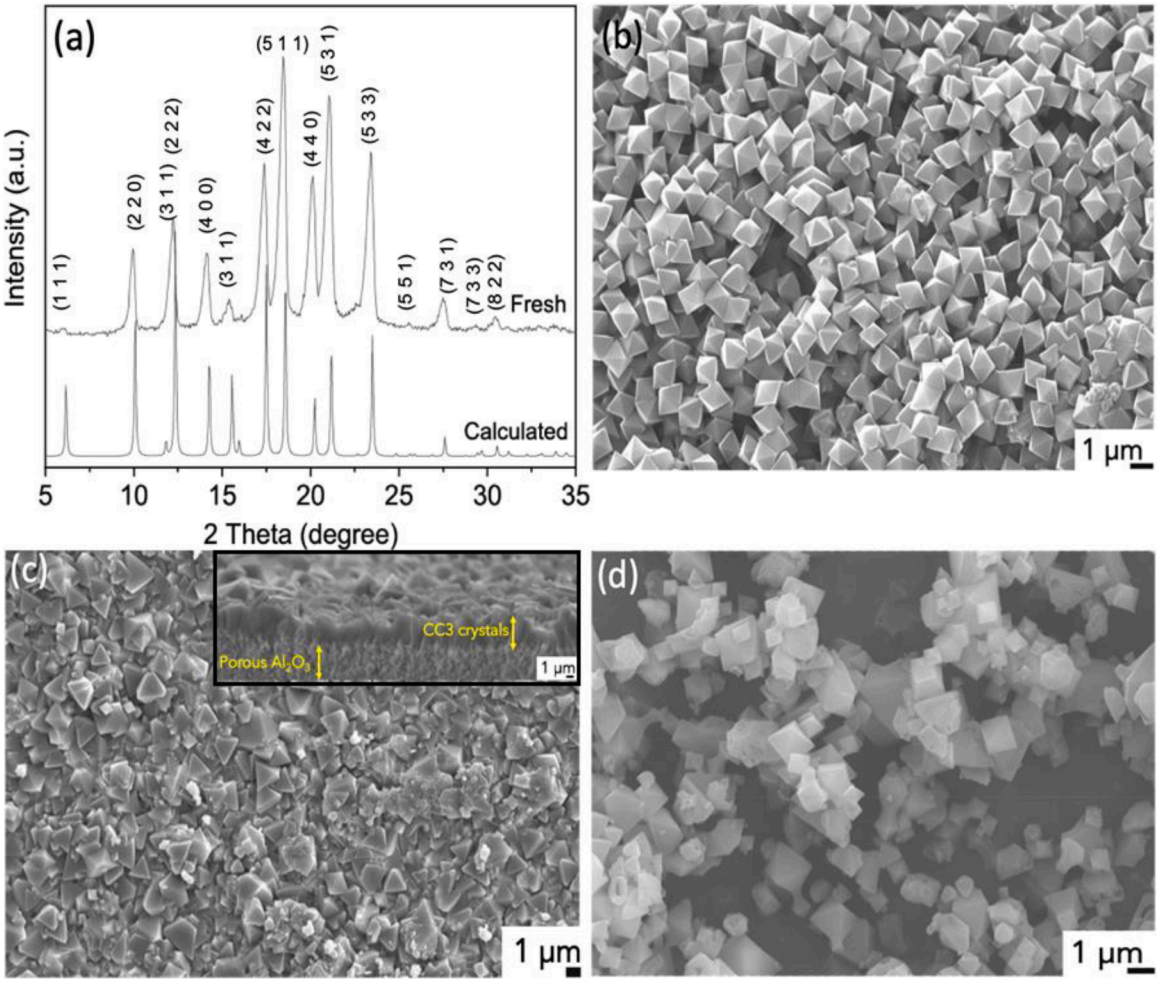

Fig. 2. (a) Experimental XRD and simulated XRD patterns of CC3 crystals; (b) SEM images of the CC3 crystals; (c) the CC3 membrane with the inset cross-section view; and (d) the spent CC3 crystals.

crystallinity was calculated for the leading peak in CC3α, at $2\theta = 6.2°$, to determine the crystallinity of the prepared CC3 with assembly time. Whereby, a sample prepared by a batch synthesis, [35] was used as a standard for 100% crystallinity. The detail for the XRD simulation can be found in the Supporting Information. The simulated results confirm the good crystallinity of the CC3 crystals. Intriguingly, Fig. 2**(b)** displays well-defined octahedral crystals with a homogenous size of around 500 nm for the edges. Such dielectric homogeneous size single octahedrons are expected to offer protective effects for the ammonia product as they would partly prevent plasma to touch ammonia molecules absorbed on the underneath side. The SAPO-34 sample displayed large cubic morphology with size in a range of 1–4 μm while the ZIF-8 and ZIF-67 samples present no centrosymmetric cubic morphology with particle size in the range of 200 nm–5 μm and 50–100 nm, respectively (**Figure S2**). The XRD patterns of the zeolite and ZIFs also confirmed their respective crystallinity (**Figure S2**). Fig. 2**(c)** presents the CC3 membrane surface consisting of CC3 octahedral crystals layers with a relatively homogeneous size distribution. The CC3 membrane layer had a thickness of around 2 μm (inset, Fig. 2**(c))**. The top surface entails crystal growth of both small and large crystals and membrane continuity. The crystals observed at the membrane surface were slightly different from the single CC3 crystals as depicted in Fig. 2**(b),** indicating that the secondary seeded growth employed for membrane synthesis encouraged heterogeneous nucleation on the support surface followed by recrystallization. The N_2 adsorption-desorption isotherm curve of the CC3 crystals indicates the existence of micropores (**Figure S3**), which is also confirmed by the pore size values (**Table S2**). The BET specific surface area of the SAPO-34, ZIF-8, ZIF-67, and CC3 samples was 557, 1880, 1674, and 443 m^2/g, respectively.

The stability of the CC3 crystals cannot be compared with similar research as no work was available when employing CC3 for ammonia synthesis at the time when this paper is written. Nonetheless, the SEM image of the CC3 sample spent over the DBD plasma reactor for 10 h (Fig. 2**(d)**) still displayed well-defined octahedral crystals while its XRD pattern also presented an insignificant difference from its fresh one (**Figure S4**). Such observations demonstrate the good stability and great potential for recycling the CC3. Stemming from these results, this work recycled the spent CC3 and re-used the recycled CC3 catalyst for ammonia synthesis under plasma. The results will be discussed in the next section. Remarkably, the reused CC3 membranes (after plasma exposure) kept their morphological features confirming their structural stability (**Figure S5**).

3.2. *Ammonia synthesis performance*

The performance of the CC3 single crystals and the CC3 membrane was evaluated *via* the ammonia synthesis rate and the results are shown in Fig. 3. The ammonia synthesis performance over the empty DBD reactor was also performed to highlight the effects of the packed CC3 crystals on the ammonia synthesis rate. Fig. 3(a). displays that a relatively low ammonia synthesis rate of 0.38 μmol min^{-1} was obtained over the empty reactor while the presence of CC3 resulted in six times higher ammonia synthesis rate with 2.2 μmol min^{-1} produced. In the absence of the packing, the formation of ammonia involves the chain reactions in the plasma gas phase and the surface reactions on the tungsten electrode and the reactor wall (wall effects), which cannot be overlooked[36]. Due to distinction between their reactor configuration and operational parameters like filamentary discharge versus bulk discharge. The comparison was performed in terms of μmol of ammonia produced per min, as shown Fig. 3(a) for a rationale evaluation in the determination of

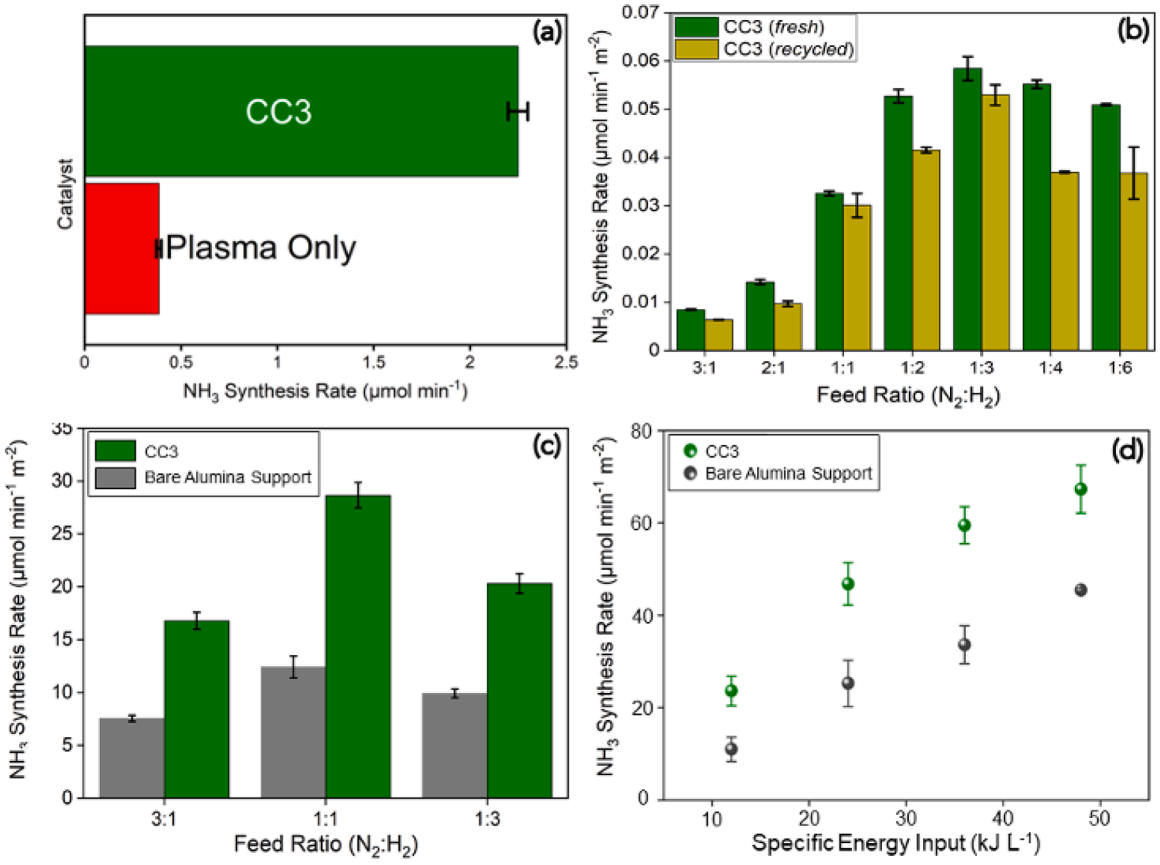

Fig. 3. Ammonia synthesis rate obtained over the (a) DBD reactor with CC3 packed at a fixed input flowrate of N_2:H_2 of 1:3; and (b) at different feed ratios at a plasma power of 5 W. Ammonia synthesis rate obtained over plasma membrane reactor at various feed ratio (c) at a plasma power of 5 W; and (d) with bare alumina support and CC3 membrane at various specific input energy (SEI). The details of the SEI calculation are presented in the Supplementary Material.

catalytic activity between absence and CC3 Packed Bed reactor. Further, the voltage-charge analysis of the empty DBD reactor indicated a quantitatively lower charge density relative to the CC3 packed-bed counterpart at similar voltages (Figure S6). This result further supports the higher ammonia synthesis rate obtained when using the CC3 crystals. A similar observation was reported previously when using ZIFs [20]. In the meanwhile, the ammonia synthesis rate produced over the CC3 in the packed-bed reactor and in membrane forms were evaluated on their respective active surface at different feed ratios i.e., nitrogen-rich to hydrogen-rich. As shown in Fig. 3(b), the maximum ammonia synthesis rate was observed at a 1:3 (N_2:H_2) ratio. To evaluate the reuse ability of the spent CC3 catalyst for plasma-driven ammonia synthesis, in this work, we recycled the spent CC3 catalysts by heating the spent samples in the furnace at 90 °C for 5 min under a continuous flow of N_2. The observed results exhibited that the recycled CC3 catalyst owning great potential for its re-use capacity Fig. 3(b). Whereby, the recycled CC3 sample showed a slight reduction of catalytic performance compared to the fresh sample. For instance, at a feed ratio of 1:3, the recycled CC3 catalyst displayed an ammonia synthesis rate of around 0.05 μmol min^{-1} m^{-2}, which is slightly lower than the fresh sample (about 0.06 μmol min^{-1} m^{-2}). The surface area of the reused CC3 sample decreased from 443 to 352 m^2/g. In addition, the observed reduction in the catalytic performance of the recycled CC3 catalyst (as compared to the fresh catalysts) may be related to the structural local disorder after plasma exposure, deriving from the collision between electrons and the catalyst surface in the plasma. We also observed a slight increase of the XRD intensity at low angles (2 theta below of 10°), suggesting a negligible local disorder of the CC3 structure (Figure S4). Further, the SEM images of the spent CC3 catalyst displayed a gentle increment of the CC3 crystal size (Fig. 2(d)). In short, the CC3 catalyst exhibited a good stability over the plasma-assisted ammonia synthesis for at least 10 h and even by a simple recycle process, excellent ammonia synthesis rate was still maintained over the recycled CC3 catalyst. These results reveal a promising potential for the re-use of catalysts spent over plasma-assisted chemical reactions.

The ammonia synthesis performance for the CC3 membrane was evaluated in a unique membrane reactor developed uniquely by our group. Experiments with both bare porous cylindrical alumina support and the CC3 membrane grown on the inner surface of the porous cylindrical alumina support were performed at different flow ratios 1:1, 1:3, and 3:1 (N_2:H_2). This to determine the effect of the alumina support and to benchmark the CC3 membrane activity. For direct comparison, all the experiments for the bare alumina support and CC3 membrane on the alumina support were replicated at the same flow and electrical conditions. Fig. 3**(c)** shows the catalytic data for the cylindrical bare alumina support and the alumina cylindrical support with the CC3 membrane. As it can be observed the equimolar feed ratio condition elevated the ammonia production. At a similar condition, the bare alumina support delivered an ammonia synthesis rate of 12.4 μmol min^{-1} m^{-2} while the CC3 membrane supported on alumina offered an ammonia synthesis rate of about 2 times higher than bare aluminum support, namely 28.6 μmol min^{-1} m^{-2}. In addition, the higher SEI led to a higher ammonia synthesis rate (Fig. 3**(d)**). Whereby, the ammonia synthesis rate gained over the bare alumina support increased from 10.0 to 40.5 μmol min^{-1} m^{-2} while that produced over the CC3 membrane climbed from 22.3 to 67.3 μmol min^{-1} m^{-2} when increasing the SEI from 12 to 50 kJ L^{-1} at a feed ratio (N_2:H_2) of 1:3. In general, the presence of the CC3 membrane outperformed the bare alumina by an approximately 2 factor. It should be noticed that the CC3 membrane reactor delivered a maximum ammonia synthesis rate at a feed ratio (N_2:H_2) of 1:1 (Fig. 3**(c)**) while the DBD reactor packed with CC3 crystals production peaked at a 1:3 ratio (Fig. 3**(b)**). Given the lower dissociation energy of the H_2 molecule relative to N_2, the presence of H* species is more important favoring recombination to form H_2. This can lead to a decline in the ammonia synthesis rate when a further increase in H_2 occurs, for example at N_2:H_2 of 1:4, as displayed in (Fig. 3**(b)**). This observation has been reported by other groups as well[37, 38]. In the membrane reactor, the same trend is observed, with lower ammonia synthesis rates at hydrogen-rich conditions. In this case, the excessive presence of hydrogen led to both alumina pores and the CC3 membrane being occupied by hydrogen adatoms. Such dominant existence of H* species in small pores promotes recombination and limits the diffusion of N_2*, and consequently, hinders the ammonia synthesis rate.

To benchmark the catalytic activity of CC3, the ammonia synthesis performance over the SAPO-34, ZIF-6, and ZIF-67 samples at different plasma powers was also evaluated and the results are shown in Fig. 4. The CC3 crystals delivered the highest ammonia synthesis rate followed by the SAPO-34, ZIF-8, and ZIF-67 catalyst. Accordingly, the ammonia synthesis rate obtained over the CC3, SAPO-34, ZIF-8, and ZIF-67 at a plasma power of 5 W (corresponding to the SEI of 12 kJ L^{-1}) was 0.06, 0.018, 0.014, and 0.016 μmol min^{-1} m^{-2}, respectively. Moreover, the increment in the plasma power i.e., 10 W resulted in the increase in the ammonia synthesis rate observed from all the catalyst samples. It is worth noting that the CC3 does not contain active metals. Despite this, its ammonia synthesis performance was better than the ZIFs, which contain transitional metals such as Zn and Co. This observation signifies that the ammonia synthesis rate is not dependent on the active metals at the here tested plasma conditions. But the morphology and the interactions between reactants/products with the catalyst surface overcome the active site effect, which will be discussed in the next section. Such similar observations have been previously reported by our group [39]. In other words, at the prevalent conditions the CC3 crystals produced the highest ammonia amount more efficiently in energetic terms relative to other tested catalysts. In this work, the ammonia synthesis rate as a function of time was also tested at various feed ratios and a power of 5 W. The consistency of the ammonia synthesis rate over 10 h observed from all feed ratios (**Figure S7**) further confirmed the above-discussed excellent stability of the CC3 crystals.

3.3. A mechanistic insight of the plasma-assisted ammonia synthesis when employing CC3 crystals and CC3 membrane

As depicted in Fig. 3, the presence of the CC3 improved the ammonia synthesis rate over both the packed-DBD reactor and the membrane-DBD reactor significantly, indicating the dominant ammonia protective role the CC3 offers in the overall pathways. This protection offered by porous materials has been reported previously by our group when employing Ni-MOF-74[19]. It is well-accepted that NH* species are generated by plasma-induced excited species including N_2* and H*. Such NH* precursors react with hydrogen to form NH_3. Nonetheless, a strenuous challenge is the rapid decomposition of NH_3 taking place concomitantly during the reaction by excited species, resulting in the low ammonia synthesis rate and energy yield for ammonia formation in the plasma as already reported[40]. In the absence of the CC3, the empty DBD reactor resulted in a low ammonia synthesis rate of around 0.38 μmol min^{-1}. When ammonia synthesis is performed over the bare porous cylindrical alumina support, an ammonia synthesis rate of 10.0 μmol min^{-1} m^{-2} was obtained at a similar conditions. This result can be explained by the reported benefit of slightly acidic supports such as alumina for plasma synthesis of ammonia[41].

The presence of the CC3 crystals into the DBD packed plasma system intensified the ammonia synthesis of up to 0.06 μmol min^{-1} m^{-2}, higher relative to the SAPO-34 and ZIFs samples. It stands without a doubt that the nature of the studied materials including their textural properties influences the reaction pathways taking place, particularly under the plasma regime, which is sensitive to plasma-material interactions. The ZIFs containing −C=C− on the organic linker are known to be a polarizable group, which can offer the possibility of dipole–dipole interactions between the polar ammonia molecules and the polar walls [20]. Such interactions along with the small pore aperture (3.4 Å) resulted in relatively lower ammonia uptakes and low storage capacity relative to a larger one such as the case of CC3 (3.6 Å) and SAPO-34 (3.8

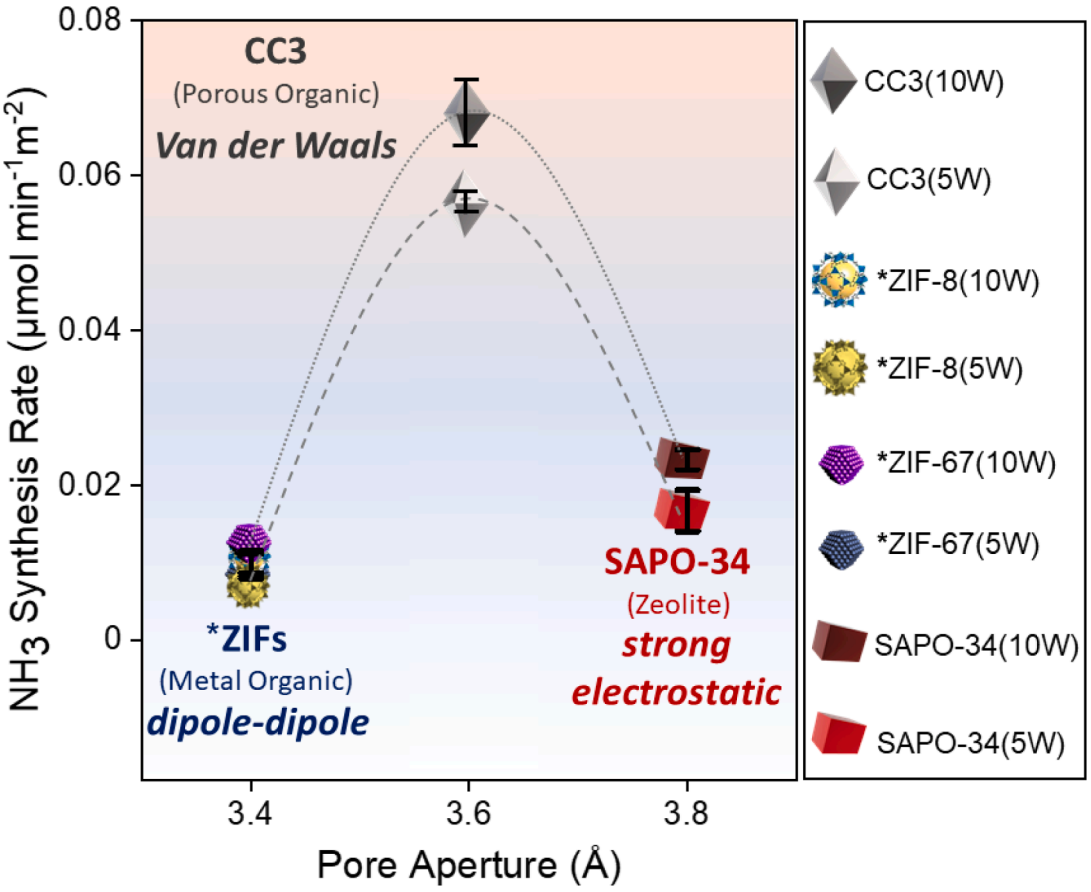

Fig. 4. Ammonia synthesis performance at as function of pore aperture and different plasma power on employed catalysts (CC3, SAPO-34 & *ZIFs[20]).

Å). Freshly generated ammonia is therefore further decomposed during the synthesis reaction. In the meantime, zeolites are reported materials that do no help in the dissociation of neither N_2 nor H_2 and in general have no activity for ammonia synthesis under thermal synthesis [42]. Nonetheless, the external surface of zeolite can interact with H and N radicals in the plasma regime, enabling the activity observed in this work. The SAPO-34 catalyst offers strong electrostatic interaction with ammonia [43], partly sieving NH_3. The CC3, on the other hand, owns a smaller pore size than the SAPO-34. Nonetheless, the CC3 delivered the highest ammonia synthesis rate relative to other catalysts in this study at similar testing conditions. We hypothesize that the homogeneous octahedral geometry of CC3 crystals plays a dominant role to protect the freshly produced ammonia molecules for further collision with plasma-induced excited species. The diffusion of the freshly formed ammonia under such dielectric octahedral CC3 crystals, particularly ammonia molecules absorbed/diffused inside the pores of underneath size resulted in the enhanced ammonia synthesis rate relative to other catalysts. Moreover, in the case of CC3, since these crystals are discreet cage molecules, they display *Van der Waals interactions* which may lead to weak intermolecular attractions between molecules. Such moderate interactions can enable adsorption-desorption steps taking place reversibly. This observation prompted our plasma membrane reactor design. However, plasma is a complex environment and other effects related to geometry on the plasma discharge, such as possible shifts of discharge mode from filamentary discharge to a surface discharge should not be disregarded[44]. It also has been indicated that materials with more uniform particle size favors surface interactions, and thereby, enhance ammonia synthesis. [40, 41] The SAPO-34, ZIF-8, and ZIF-67 samples displayed noticeably inhomogeneous particle size distribution (**Figure S2**), accounting for their lower ammonia synthesis rate relative to the CC3 catalyst. A thoughtful study on the influence of the morphology on ammonia synthesis is out of the scope of this current work; nonetheless, such primary observations reveal that the morphology of the catalyst plays an important role in ammonia synthesis under plasma. In this work, we also collected the in-situ OES spectra for the CC3 and for comparison the one for ZIF-67. Results presented in **Figure S8** show the CC3 higher intensity of the peak-related H_α species compared to the ZIF-67. The H_α species measured here are the species in the gas phase. The material with the higher amount of H atoms in the gas phase can lead to an enhanced hydrogen recombination[45]. Which restricts the binding of H atoms with Nitrogen plasma-exited species that can lead to ammonia production. The lower amount of H_α species in the gas phase for ZIF-67 is due to the "hydrogen sink" effect of the cobalt metal contained in this ZIF. Interestingly, we have observed this behavior in other porous materials when a transition metal is present[39]. This demonstrates that the porous cage CC3 contribution is not mere catalytic, but goes beyond that.

Experimental data in this work also indicated that the ammonia synthesis rate obtained when employing the CC3 membrane was 20.3 mol min^{-1} m^{-2} while for the bare porous alumina was of 10.0 µmol min^{-1} m^{-2} (as shown Fig. 3**(d)**). Which was much higher than that produced over the DBD packed with the CC3 crystals (0.06 µmol min^{-1} m^{-2}, Figure S6) at similar testing conditions. It is worth highlighting that all catalytic activity data were normalized per surface area (m^2). Although the CC3 with octahedral crystals partially protects the fresh ammonia product from the plasma, which makes it outstanding compared to other catalysts such as SAPO-34, ZIF-8, and ZIF-67; the in-situ decomposition of ammonia in the plasma still reduces the ammonia production significantly. This challenge hinders the practical applications of plasma-assisted synthesis of ammonia[46]. In this work, the alumina porous support offered a partial separation of ammonia product through its pores although the decomposition of ammonia product still

happened inside such pores. Observed from experimental and simulation results, researchers indicated that plasma discharge can penetrate the pore with size up to 50 nm though within very short times and induce short-life reactive species inside the pores[16, 47]. Kushner et al. [48], also proved that although cannot directly flow through small pores; plasma still generates a flux of photons and photoionization, which penetrates inside the sub-surface to seed plasma-induced species. The porous alumina support used in this work has a pore size of 100 nm and thereby, the presence of photons flux and photoionization induced excited species taking place inside the aluminum pores could possibly lead to the production and decomposition of ammonia taking place concomitantly. In the meanwhile, when the CC3 membrane was used, the membrane provided an enhanced separation of ammonia products (Fig. 5), and thereby, resulting in a higher ammonia synthesis rate relative to the bare porous alumina. The OES spectra for the alumina support with the CC3 membrane exhibited a weaker intensity of OES peaks of N_2^+ (391.4 nm), H_α (656.3 nm), and NH (336 nm) species, particularly for the NH species relative to the bare alumina support (without CC3 membrane) (**Figure S9**). These results further confirmed that excited species either diffused through the porous alumina support or generated inside the aluminum pores by electron flux or photoionization to form ammonia product, which was then permeated and separated from the plasma regime *via* the CC3 membrane under a continuous flow. In terms of adsorption, the CC3 crystals are discreet cage molecules and offer intermolecular attractions between molecules (**Figure S10**), which promoted ammonia adsorption and permeation. Indeed, the CC3 membrane is formed by the coordination of 1,3,5 triformylbenzene and trans 1,2 diaminocyclohexane [26]. Basic molecules like ammonia is therefore preferred to adsorb by three hydrogen bond acceptors of triformylbenzene group [49]. In principle, the diamino groups (pendant basic groups) of diaminocyclohexane should repel the basic ammonia groups. However, a full understanding of plasma separation phenomena is future work already in progress in our group.

4. Conclusions

In this work, the CC3, a prototypical porous organic cage revealed to be an effective material in crystal and membrane form for the ammonia synthesis under non thermal plasma. From the energy viewpoint, when compared with other microporous crystals such as SAPO-34, ZIF-8, and ZIF-67 having comparable pore limiting aperture, the CC3 crystals was the most efficient material, with the highest ammonia synthesis rate per m^2 (0.06 μmol min^{-1} m^{-2}) at the lowest observed SEI (12 kJ L^{-1}) and a feed ratio (N_2:H_2) of 1:3. These observations were explained by the ammonia protective effect offered by the CC3. At similar conditions, the CC3 membrane reactor developed in this work delivered an ammonia synthesis rate of 20.3 μmol min^{-1} m^{-2} and reached 28.6 μmol min^{-1} m^{-2} at an equimolar feed ratio thanks to absorption and separation role of the CC3 membrane. The results demonstrated that the in-situ isolation of fresh ammonia product from the plasma by octahedral crystals, or better with adsorption and separation by the CC3 membrane significantly suppresses ammonia decomposition by the plasma, and thereby, enhances the overall ammonia synthesis. These significant preliminary findings lead to better understanding for the factors that influence on the in-situ decomposition of fresh ammonia as well as the overall ammonia synthesis rate, to open novel avenues for the design of ammonia synthesis reactors with high efficiency under milder conditions with lower capital and operational costs.

Supplementary Material

Ammonia calibration curve; Details on the synthesis of comparative microporous crystals: SAPO-34, ZIF-8, and ZIF-67; XRD patterns and respective SEM images of the fresh SAPO-34, CC3, ZIF-8, and ZIF-67 catalysts; Nitrogen adsorption-desorption isotherms curves; Pore apertures; XRD patterns of fresh, spent, and simulated CC3 crystals; SEM images of the CC3 membranes spent over plasma-assisted ammonia synthesis. Reactor electrical characterization; Comparison on the catalytic performance of the CC3, SAPO-34, ZIF-8, and ZIF-67 for DBD

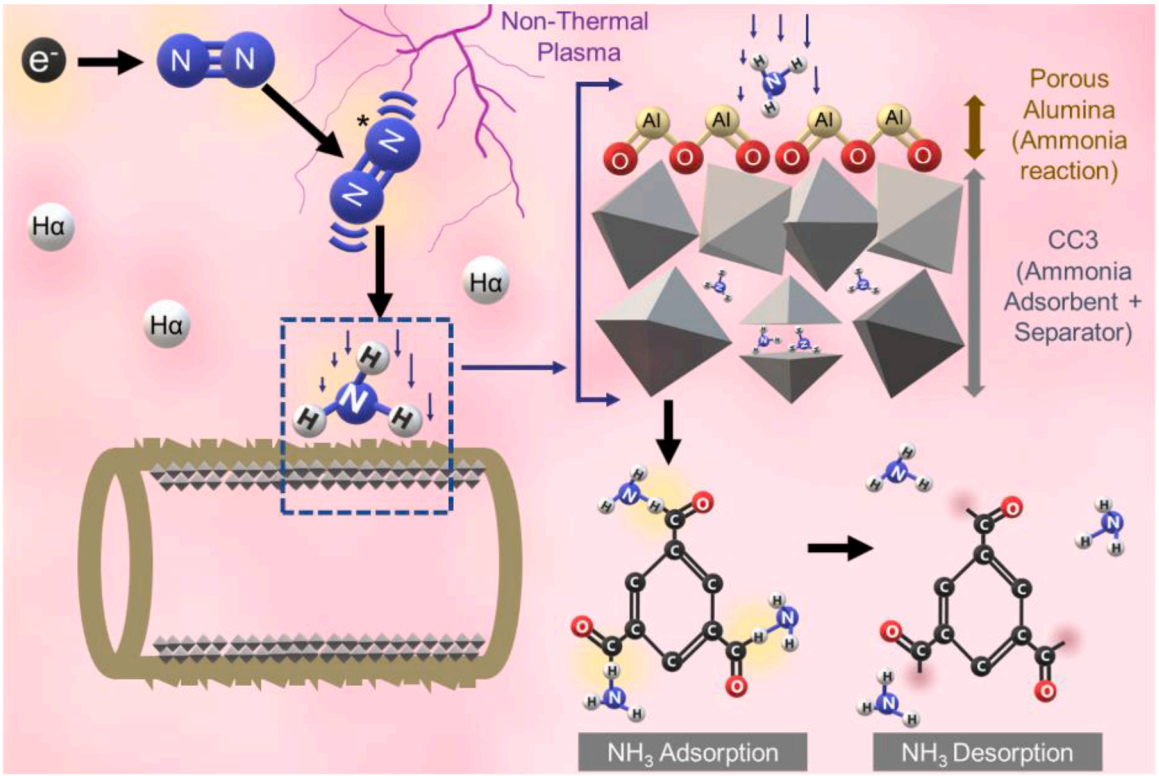

Fig. 5. Insight on the pathways for plasma-assisted ammonia synthesis over CC3 membrane.

plasma-assisted ammonia synthesis; Ammonia synthesis rate performance as a function of time over the CC3 crystal catalyst; Optical emission spectroscopy (OES) analysis on CC3 and ZIF-67; OES spectra of gas species collected during plasma – assisted ammonia synthesis over the CC3 crystals and the CC3 membrane; Ammonia adsorption.

CRediT authorship contribution statement

Fnu Gorky: Data curation, Investigation, Methodology. **Hoang M. Nguyen:** Data curation, Investigation, Methodology. **Jolie M. Lucero:** Data curation, Investigation, Methodology. **Shelby Guthrie:** Data curation, Investigation, Methodology. **James M. Crawford:** Data curation, Investigation, Methodology. **Moises A. Carreon:** Conceptualization, Supervision, Formal analysis, Funding acquisition. **Maria L. Carreon:** Conceptualization, Supervision, Formal analysis, Funding acquisition.

Declaration of Competing Interest

The authors declare that they have no known competing financial interests or personal relationships that could have appeared to influence the work reported in this paper.

Acknowledgement

Maria L. Carreon thanks NSF-CBET award No. 2203166. M.A. Carreon acknowledges Department of Energy Office of Science DE-SC0021357. We thank Prof. Manika Prasad from the Colorado School of Mines Geophysics Department for their support with adsorption measurements.

Role of the funding source

None

Supplementary materials

Supplementary material associated with this article can be found, in the online version, at doi:10.1016/j.ceja.2022.100340.

References

[1] J. Andersson, S. Grönkvist, Large-scale storage of hydrogen, Int. J. Hydrog. Energy 44 (23) (2019) 11901–11919, https://doi.org/10.1016/j.ijhydene.2019.03.063, https://doi.org/https://doi.org/.

[2] F. Chang, W. Gao, J. Guo, P. Chen, Emerging materials and methods toward ammonia-based energy storage and conversion, Adv. Mater. 33 (50) (2021), 2005721, https://doi.org/10.1002/adma.202005721 https://doi.org/https://doi.org/.

[3] D.W. Kang, J.H. Holbrook, Use of NH3 fuel to achieve deep greenhouse gas reductions from US transportation, Energy Rep. 1 (2015) 164–168, https://doi.org/10.1016/j.egyr.2015.08.001, https://doi.org/https://doi.org/.

[4] Y. Chen, B. Zhang, Y. Su, C. Sui, J. Zhang, Effect and mechanism of combustion enhancement and emission reduction for non-premixed pure ammonia combustion based on fuel preheating, Fuel 308 (2022), 122017, https://doi.org/10.1016/j.fuel.2021.122017 https://doi.org/https://doi.org/.

[5] W.F. Donkin II, On the direct synthesis of ammonia, Proc. R. Soc. Lond. 21 (139–147) (1873) 281–282, https://doi.org/10.1098/rspl.1872.0057, https://doi.org/https://doi.org/.

[6] D. Frattini, G. Cinti, G. Bidini, U. Desideri, R. Cioffi, E. Jannelli, A system approach in energy evaluation of different renewable energies sources integration in ammonia production plants, Renew. Energy 99 (2016) 472–482, https://doi.org/10.1016/j.renene.2016.07.040, https://doi.org/https://doi.org/.

[7] J.R. Shah, F. Gorky, J. Lucero, M.A. Carreon, M.L. Carreon, Ammonia synthesis via atmospheric plasma catalysis: zeolite 5A, a case of study, Ind. Eng. Chem. Res. 59 (11) (2020) 5167–5176, https://doi.org/10.1021/acs.iecr.9b05220.

[8] T. Zhang, R. Zhou, S. Zhang, R. Zhou, J. Ding, F. Li, J. Hong, L. Dou, T. Shao, A. B. Murphy, Sustainable ammonia synthesis from nitrogen and water by one-step plasma catalysis, Energy Environ. Mater. (2022), https://doi.org/10.1002/eem2.12344 https://doi.org/https://doi.org/.

[9] P. Peng, C. Schiappacasse, N. Zhou, M. Addy, Y. Cheng, Y. Zhang, K. Ding, Y. Wang, P. Chen, R. Ruan, Sustainable non-thermal plasma-assisted nitrogen fixation—synergistic catalysis, ChemSusChem 12 (16) (2019) 3702–3712, https://doi.org/10.1002/cssc.201901211, https://doi.org/https://doi.org/.

[10] S. Dou, L. Tao, R. Wang, S. El Hankari, R. Chen, S. Wang, Plasma-assisted synthesis and surface modification of electrode materials for renewable energy, Adv. Mater. 30 (21) (2018), 1705850, https://doi.org/10.1002/adma.201705850 https://doi.org/https://doi.org/.

[11] A. Bogaerts, E.C. Neyts, Plasma technology: an emerging technology for energy storage, ACS Energy Lett. 3 (4) (2018) 1013–1027, https://doi.org/10.1021/acsenergylett.8b00184, https://doi.org/https://doi.org/.

[12] J.R. Shah, F. Gorky, J. Lucero, M.A. Carreon, M.L. Carreon, Ammonia synthesis via atmospheric plasma catalysis: zeolite 5A, a case of study, Ind. Eng. Chem. Res. 59 (11) (2020) 5167–5176, https://doi.org/10.1021/acs.iecr.9b05220, https://doi.org/https://doi.org/.

[13] D. Zhou, R. Zhou, R. Zhou, B. Liu, T. Zhang, Y. Xian, P.J. Cullen, X. Lu, K. K. Ostrikov, Sustainable ammonia production by non-thermal plasmas: status, mechanisms, and opportunities, Chem. Eng. J. 421 (2021), 129544, https://doi.org/10.1016/j.cej.2021.129544 https://doi.org/https://doi.org/.

[14] P. Barboun, P. Mehta, F.A. Herrera, D.B. Go, W.F. Schneider, J.C. Hicks, Distinguishing plasma contributions to catalyst performance in plasma-assisted ammonia synthesis, ACS Sustain. Chem. Eng. 7 (9) (2019) 8621–8630, https://doi.org/10.1021/acssuschemeng.9b00406, https://doi.org/https://doi.org/.

[15] L. Hollevoet, F. Jardali, Y. Gorbanev, J. Creel, A. Bogaerts, J.A. Martens, Towards green ammonia synthesis through plasma-driven nitrogen oxidation and catalytic reduction, Angew. Chem. Int. Ed. 132 (52) (2020) 24033–24037, https://doi.org/10.1002/ange.202011676, https://doi.org/https://doi.org/.

[16] A. Bogaerts, Q.-.Z. Zhang, Y.-.R. Zhang, K. Van Laer, W. Wang, Burning questions of plasma catalysis: answers by modeling, Catal. Today 337 (2019) 3–14, https://doi.org/10.1016/j.cattod.2019.04.077, https://doi.org/https://doi.org/.

[17] P. Navascués, J.M. Obrero-Pérez, J. Cotrino, A.n.R. González-Elipe, A. Gómez-Ramírez, Unraveling discharge and surface mechanisms in plasma-assisted ammonia reactions, ACS Sustain. Chem. Eng. 8 (39) (2020) 14855–14866, https://doi.org/10.1021/acssuschemeng.0c04461, https://doi.org/https://doi.org/.

[18] P. Navascués, J.M. Obrero-Pérez, J. Cotrino, A.R. González-Elipe, A. Gómez-Ramírez, Isotope labelling for reaction mechanism analysis in DBD plasma processes, Catalysts 9 (1) (2019) 45, https://doi.org/10.3390/catal9010045, https://doi.org/https://doi.org/.

[19] J. Shah, T. Wu, J. Lucero, M.A. Carreon, M.L. Carreon, Nonthermal plasma synthesis of ammonia over Ni-MOF-74, ACS Sustain. Chem. Eng. 7 (1) (2018) 377–383, https://doi.org/10.1021/acssuschemeng.8b03705, https://doi.org/https://doi.org/.

[20] F. Gorky, J.M. Lucero, J.M. Crawford, B. Blake, M.A. Carreon, M.L. Carreon, Plasma-induced catalytic conversion of nitrogen and hydrogen to ammonia over zeolitic imidazolate frameworks ZIF-8 and ZIF-67, ACS Appl. Mater. Interfaces 13 (18) (2021) 21338–21348, https://doi.org/10.1021/acsami.1c03115, https://doi.org/https://doi.org/.

[21] F. Gorky, M.A. Carreon, M.L. Carreon, Experimental strategies to increase ammonia yield in plasma catalysis over LTA and BEA zeolites, IOP SciNotes 1 (2) (2020), 024801, https://doi.org/10.1088/2633-1357/aba1f8 https://doi.org/https://doi.org/.

[22] Q. Wei, J.M. Lucero, J.M. Crawford, J.D. Way, C.A. Wolden, M.A. Carreon, Ammonia separation from N2 and H2 over LTA zeolitic imidazolate framework membranes, J. Membr. Sci. 623 (2021), 119078, https://doi.org/10.1016/j.memsci.2021.119078 https://doi.org/https://doi.org/.

[23] J.T.A. Jones, T. Hasell, X. Wu, J. Bacsa, K.E. Jelfs, M. Schmidtmann, S.Y. Chong, D. J. Adams, A. Trewin, F. Schiffman, Modular and predictable assembly of porous organic molecular crystals, Nature 474 (7351) (2011) 367–371, https://doi.org/10.1038/nature10125, https://doi.org/https://doi.org/.

[24] T. Tozawa, J.T.A. Jones, S.I. Swamy, S. Jiang, D.J. Adams, S. Shakespeare, R. Clowes, D. Bradshaw, T. Hasell, S.Y. Chong, Porous organic cages, Nat. Mater. 8 (12) (2009) 973–978, https://doi.org/10.1038/nmat2545, https://doi.org/https://doi.org/.

[25] Q. Song, S. Jiang, T. Hasell, M. Liu, S. Sun, A.K. Cheetham, E. Sivaniah, A.I. Cooper, Porous organic cage thin films and molecular-sieving membranes, Adv. Mater. 28 (13) (2016) 2629–2637, https://doi.org/10.1002/adma.201505688, https://doi.org/https://doi.org/.

[26] L. Chen, P.S. Reiss, S.Y. Chong, D. Holden, K.E. Jelfs, T. Hasell, M.A. Little, A. Kewley, M.E. Briggs, A. Stephenson, Separation of rare gases and chiral molecules by selective binding in porous organic cages, Nat. Mater. 13 (10) (2014) 954–960, https://doi.org/10.1038/nmat4035, https://doi.org/https://doi.org/.

[27] M. Liu, M.A. Little, K.E. Jelfs, J.T.A. Jones, M. Schmidtmann, S.Y. Chong, T. Hasell, A.I. Cooper, Acid-and base-stable porous organic cages: shape persistence and pH stability via post-synthetic "tying" of a flexible amine cage, J. Am. Chem. Soc. 136 (21) (2014) 7583–7586, https://doi.org/10.1021/ja503223j, https://doi.org/https://doi.org/.

[28] T. Hasell, M. Miklitz, A. Stephenson, M.A. Little, S.Y. Chong, R. Clowes, L. Chen, D. Holden, G.A. Tribello, K.E. Jelfs, Porous organic cages for sulfur hexafluoride separation, J. Am. Chem. Soc. 138 (5) (2016) 1653–1659, https://doi.org/10.1021/jacs.5b11797, https://doi.org/https://doi.org/.

[29] S. Jiang, Q. Song, A. Massey, S.Y. Chong, L. Chen, S. Sun, T. Hasell, R. Raval, E. Sivaniah, A.K. Cheetham, Oriented two-dimensional porous organic cage crystals, Angew. Chem. Int. Ed. 129 (32) (2017) 9519–9523, https://doi.org/10.1002/anie.201704579, https://doi.org/https://doi.org/.

[30] J.M. Lucero, M.A. Carreon, Separation of light gases from xenon over porous organic cage membranes, ACS Appl. Mater. Interf. 12 (28) (2020) 32182–32188, https://doi.org/10.1021/acsami.0c08040, https://doi.org/https://doi.org/.

[31] X. Feng, Z. Zong, S.K. Elsaidi, J.B. Jasinski, R. Krishna, P.K. Thallapally, M. A. Carreon, Kr/Xe separation over a chabazite zeolite membrane, J. Am. Chem. Soc. 138 (31) (2016) 9791–9794, https://doi.org/10.1021/jacs.6b06515, https://doi.org/https://doi.org/.

[32] T. Wu, X. Feng, S.K. Elsaidi, P.K. Thallapally, M.A. Carreon, Zeolitic imidazolate framework-8 (ZIF-8) membranes for Kr/Xe separation, Ind. Eng. Chem. Res. 56 (6) (2017) 1682–1686, https://doi.org/10.1021/acs.iecr.6b04868, https://doi.org/https://doi.org/.

[33] J. Qian, F. Sun, L. Qin, Hydrothermal synthesis of zeolitic imidazolate framework-67 (ZIF-67) nanocrystals, Mater. Lett. 82 (2012) 220–223, https://doi.org/10.1016/j.matlet.2012.05.077, https://doi.org/https://doi.org/.

[34] S. Denning, J.M. Lucero, A.A.A. Majid, J.M. Crawford, M.A. Carreon, C.A. Koh, Porous organic cage CC3: an effective promoter for methane hydrate formation for natural gas storage, J. Phys. Chem. C 125 (37) (2021) 20512–20521, https://doi.org/10.1021/acs.jpcc.1c04657.

[35] J. Lucero, S.K. Elsaidi, R. Anderson, T. Wu, D.A. Gómez-Gualdrón, P.K. Thallapally, M.A. Carreon, Time dependent structural evolution of porous organic cage CC3, Cryst. Growth Des. 18 (2) (2018) 921–927, https://doi.org/10.1021/acs.cgd.7b01405, https://doi.org/https://doi.org/.

[36] T.-.W. Liu, F. Gorky, M.L. Carreon, D.A. Gómez-Gualdrón, Energetics of reaction pathways enabled by N and H radicals during catalytic, plasma-assisted NH3 synthesis, ACS Sustain. Chem. Eng. (2022), https://doi.org/10.1021/acssuschemeng.1c05660 https://doi.org/https://doi.org/.

[37] M. Kitano, Y. Inoue, Y. Yamazaki, F. Hayashi, S. Kanbara, S. Matsuishi, T. Yokoyama, S.-.W. Kim, M. Hara, H. Hosono, Ammonia synthesis using a stable electride as an electron donor and reversible hydrogen store, Nat. Chem. 4 (11) (2012) 934–940, https://doi.org/10.1038/nchem.1476, https://doi.org/https://doi.org/.

[38] J. Huang, M. Yuan, X. Li, Y. Wang, M. Li, J. Li, Z. You, Inhibited hydrogen poisoning for enhanced activity of promoters-Ru/Sr2Ta2O7 nanowires for ammonia synthesis, J. Catal. 389 (2020) 556–565, https://doi.org/10.1016/j.jcat.2020.06.037, https://doi.org/https://doi.org/.

[39] S. Gershman, H. Fetsch, F. Gorky, M.L. Carreon, arXiv preprint, 2022, https://doi.org/10.48550/arXiv.2201.11858.

[40] Y. Wang, M. Craven, X. Yu, J. Ding, P. Bryant, J. Huang, X. Tu, Plasma-enhanced catalytic synthesis of ammonia over a Ni/Al2O3 catalyst at near-room temperature: insights into the importance of the catalyst surface on the reaction mechanism, ACS Catal. 9 (12) (2019) 10780–10793, https://doi.org/10.1021/acscatal.9b02538, https://doi.org/https://doi.org/.

[41] F. Gorky, A. Best, J. Jasinski, B.J. Allen, A.C. Alba-Rubio, M.L. Carreon, Plasma catalytic ammonia synthesis on Ni nanoparticles: the size effect, J. Catal. 393 (2021) 369–380, https://doi.org/10.1016/j.jcat.2020.11.030, https://doi.org/https://doi.org/.

[42] A. Itadani, M. Tanaka, T. Mori, H. Torigoe, H. Kobayashi, Y. Kuroda, Potential for fixation of N_2 at room temperature utilizing a copper-ion-exchanged MFI-type zeolite as an adsorbent: evaluation of the bond dissociation energy of adsorbed N N and the bond strength of the Cu^{+}N(N) species, J. Phys. Chem. Lett. 1 (15) (2010) 2385–2390, https://doi.org/10.1021/jz100467w.

[43] A. Itadani, M. Tanaka, T. Mori, H. Torigoe, H. Kobayashi, Y. Kuroda, Potential for fixation of N2 at room temperature utilizing a copper-ion-exchanged MFI-type zeolite as an adsorbent: evaluation of the bond dissociation energy of adsorbed N N and the bond strength of the Cu+-N(N) species, J. Phys. Chem. Lett. 1 (15) (2010) 2385–2390, https://doi.org/10.1021/jz100467w, https://doi.org/https://doi.org/.

[44] K.H.R. Rouwenhorst, Y. Engelmann, K. van't Veer, R.S. Postma, A. Bogaerts, L. Lefferts, Plasma-driven catalysis: green ammonia synthesis with intermittent electricity, Green Chem 22 (19) (2020) 6258–6287, https://doi.org/10.1039/D0GC02058C, https://doi.org/https://doi.org/.

[45] J. Shah, F. Gorky, P. Psarras, B. Seong, D.A. Gómez-Gualdrón, M.L. Carreon, Enhancement of the yield of ammonia by hydrogen-sink effect during plasma catalysis, ChemCatChem 12 (4) (2020) 1200–1211, https://doi.org/10.1002/cctc.201901769, https://doi.org/https://doi.org/.

[46] K.H.R. Rouwenhorst, S. Mani, L. Lefferts, Improving the energy yield of plasma-based ammonia synthesis with in situ adsorption, ACS Sustain. Chem. Eng. (2022), https://doi.org/10.1021/acssuschemeng.1c08467 https://doi.org/https://doi.org/.

[47] Q.-.Z. Zhang, A. Bogaerts, Propagation of a plasma streamer in catalyst pores, Plasma Sources Sci. Technol. 27 (3) (2018), 035009, https://doi.org/10.1088/1361-6595/aab47a https://doi.org/https://doi.org/.

[48] K. Konina, J. Kruszelnicki, M.J. Kushner, Atmospheric pressure plasma treatment of porous dielectrics, 2020, p. XF4.008.

[49] B.D. Egleston, M.C. Brand, F. Greenwell, M.E. Briggs, S.L. James, A.I. Cooper, D. E. Crawford, R.L. Greenaway, Continuous and scalable synthesis of a porous organic cage by twin screw extrusion (TSE), Chem. Sci. 11 (25) (2020) 6582–6589, https://doi.org/10.1039/D0SC01858A, https://doi.org/https://doi.org/.